Article

Integration of Optical and Synthetic Aperture Radar Data with Different Synthetic Aperture Radar Image Processing Techniques and Development Stages to Improve Soybean Yield Prediction

Isabella A. Cunha [1], Gustavo M. M. Baptista [2], Victor Hugo R. Prudente [3], Derlei D. Melo [1] and Lucas R. Amaral [1,*]

1 School of Agricultural Engineering, University of Campinas—UNICAMP, Campinas 13083-875, SP, Brazil; isabella.cunha@feagri.unicamp.br (I.A.C.)
2 Institute of Geoscience, University of Brasília, Brasília 70910-900, DF, Brazil
3 School for Environment and Sustainability, University of Michigan, Ann Arbor, MI 48109, USA; victorrp@umich.edu
* Correspondence: lucas.amaral@feagri.unicamp.br

Abstract: Predicting crop yield throughout its development cycle is crucial for planning storage, processing, and distribution. Optical remote sensing has been used for yield prediction but has limitations, such as cloud interference and only capturing canopy-level data. Synthetic Aperture Radar (SAR) complements optical data by capturing information even in cloudy conditions and providing additional plant insights. This study aimed to explore the correlation of SAR variables with soybean yield at different crop stages, testing if SAR data enhances predictions compared to optical data alone. Data from three growing seasons were collected from an area of 106 hectares, using eight SAR variables (Alpha, Entropy, DPSVI, RFDI, Pol, RVI, *VH*, and *VV*) and four speckle noise filters. The Random Forest algorithm was applied, combining SAR variables with the EVI optical index. Although none of the SAR variables showed strong correlations with yield (r < |0.35|), predictions improved when SAR data were included. The best performance was achieved using DPSVI with the Boxcar filter, combined with EVI during the maturation stage (with EVI:RMSE = 0.43, 0.49, and 0.60, respectively, for each season; while EVI + DPSVI:RMSE = 0.39, 0.49, and 0.42). Despite improving predictions, the computational demands of SAR processing must be considered, especially when optical data are limited due to cloud cover.

Keywords: precision agriculture; SAR vegetation index; backscatter coefficient; polarimetric decomposition; EVI; machine learning

1. Introduction

Research has increasingly focused on maximizing quality and productivity while minimizing the consumption of agricultural inputs and water resources, acknowledging the limitations of natural resources [1]. In this context, predicting the productivity of an agricultural crop enables the planning of the entire production chain, both at the national and field levels, allowing for better control over price speculation; more efficient use of storage, operational, and logistical resources; and improved planning for commercialization [2,3]. It also provides essential information for agricultural management adjustments and validation of treatments. In this scenario, Precision Agriculture (PA) uses techniques and technologies to maximize crop productivity, reduce costs and input usage, and manage field variability. Among the technologies used in PA, remote sensing stands out, providing information on the interaction of solar electromagnetic radiation with targets on the Earth's surface [4]. These data have been widely used to monitor crop development, investigate potential issues, and predict agricultural productivity [5,6], with some techniques allowing yield prediction while the crop is still growing [7].

The popularization of knowledge about optical remote sensing has enabled the acquisition of information about agricultural crops by data from spectral bands and vegetation indices. These data are provided by platforms that acquire sensor data from satellites, such as the Landsat and Sentinel-2 series [8]. However, data collection by these optical sensors is limited due to cloud interference and the inability to capture images at night [9]. In Brazil, optical remote sensing is already widely used in agricultural applications. Nevertheless, the planting window for some crops, such as soybean, occurs during rainy and cloudy periods, which reduces the availability of high-quality data throughout the soybean growth development [10,11].

The Synthetic Aperture Radar (SAR) sensor, on the other hand, operates in the microwave range of electromagnetic wavelengths, where, depending on the wavelength, there is minimal atmospheric attenuation [4], allowing data collection from agricultural areas even under cloudy conditions or at night. The availability of free data and its temporal resolution have sparked interest in studies using SAR sensors since the launch of Sentinel-1 in 2014. Although it operates in the C-band and has penetration limitations in the canopy due to its intensity, it provides complementary information to optical sensors [12]. The SAR signal response is sensitive to plant structure (size, shape, and orientation of leaves, stems, and fruits) as well as the water volume in the vegetation canopy (at the molecular level) [13,14]. Additionally, as with optical remote sensing, SAR vegetation indices allow for more efficient crop information acquisition. Thus, radar sensing can generate different images that relate in some way to the plant canopy.

Moreover, different results can be obtained from distinct SAR image preprocessing techniques. These various SAR preprocessing have been used for agricultural purposes, such as identifying phenological stages [15], crop monitoring [13,16], crop mapping and classification [13,17], as well as estimating and predicting crop yields [18]. However, SAR images have inherent noise: speckle noise, caused by the interaction of electromagnetic waves with the Earth's surface and the way the data is reflected to the sensor [19,20]. Nonetheless, various available filters can mitigate this noise when applied, but there are no studies using different speckle noise filters for yield prediction in soybean crops. In addition to speckle noise, the use of SAR data for agricultural fields faces challenges due to the interference of canopy moisture, planting row orientation, and soil properties. Furthermore, SAR images require complex processing, demanding high computational costs.

Optical remote sensing is already widely used to obtain yield prediction information [21,22]. However, optical sensor data only capture the energy reflected from the top of the canopy and are affected by clouds, whereas radar parameters can capture information below the canopy top and are sensitive to canopy geometry and moisture, which can be used to assist in crop yield prediction [14]. Recent studies, such as those conducted by Hosseini et al. [23], Mestre-Quereda et al. [17], and Hashemi et al. [24], have highlighted the potential of SAR images to improve crop yield prediction performance when integrated with optical data. Hosseini et al. [23] achieved better soybean yield prediction performance at the field level by integrating optical vegetation indices and SAR images ($r^2 = 0.85$) compared to using only optical indices ($r^2 = 0.65$). Despite advancements in integrating optical and radar remote sensing for soybean yield prediction, a substantial gap remains in exploring different processing techniques and incorporating SAR vegetation indices for field-level predictions. Identifying the most effective input data can boost predictive performance and refine remote sensing-generated models. Additionally, determining optimal processing approaches for SAR images is crucial for enhancing efficiency and accuracy, as these images require complex processing and involve high computational costs. By finding more effective methods, we can not only improve prediction accuracy and increase reliability for data users but also make better use of available resources. Therefore, the objectives of this study were: (1) to explore the correlation of different SAR variables with soybean yield using different types of speckle noise filters at different stages of crop development; and (2) to test whether the use of these SAR variables improves soybean yield prediction performance compared to the exclusive use of optical remote sensing using EVI.

2. Materials and Methods

2.1. Experimental Site and Yield Data

This study was conducted in a commercial soybean production area of approximately 106 hectares, consisting of 10 fields (Figure 1). The area is located in the municipality of Cosmópolis, in the interior of the state of São Paulo, Brazil. The experimental data consist of dry soybean grain yield (t/ha) from three growing harvests. In the first and second harvests, the M5917 IPRO (Itaberá, São Paulo, Brazil) cultivar was used, while in the third harvest, the NS5933 IPRO (Pato Branco, Paraná, Brazil) and Coliseu 631X65 RSF12X (Pato Branco, Paraná, Brazil) cultivars were used. The cultivars exhibit medium branching intensity in the first two harvests and medium to high in the third. These data were obtained using a yield monitor installed on the harvester. The monitor components were inspected before harvesting, and after the completion of the study site's harvest, the amount of grain collected was recorded in the monitor to determine the calibration factor, adjusting all datasets to reflect a realistic grain yield. Even with calibration, it is essential to review the entire dataset and eliminate any unrealistic data and some errors. To reduce errors and inconsistencies in the data, the procedure suggested by Maldaner et al. [25] was adopted.
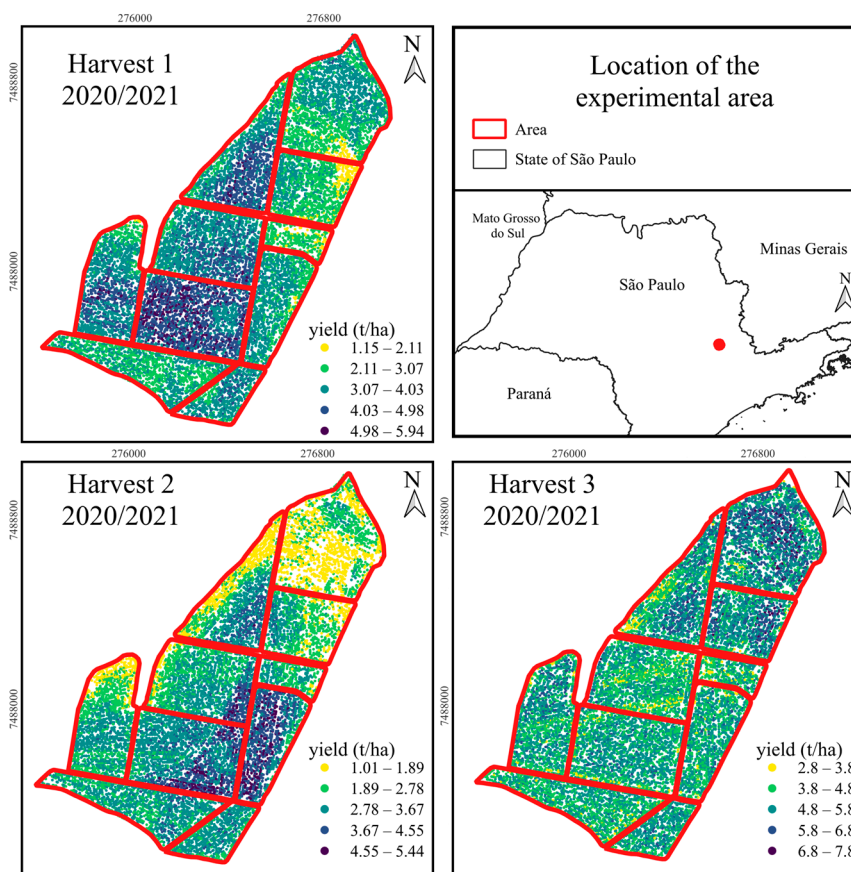

Figure 1. Experimental area with field boundaries marked in red and soybean yield data points in each harvest.

2.2. Remote Sensing Data

SAR data were collected from Sentinel-1, which operates in the C-band at a frequency of 5.405 GHz, corresponding to a wavelength of approximately 5.55 cm. The SAR data were acquired at the GRD (Ground Range Detected) level in IW (Interferometric Wide Swath) mode to obtain backscatter coefficients. Additionally, SAR data were acquired at the SLC (Single Look Complex) level 1 in the same IW mode for polarimetric decomposition processing. The spatial resolution is 5×20 m for SLC data and 10 m for GRD data. The

mode used provided dual-polarization data: *VH* (vertically polarized waves emitted and horizontally polarized waves received) and *VV* (vertically polarized waves emitted and vertically polarized waves received).

Optical images were used from the Sentinel-2A/B satellite constellation, captured by the Multispectral Instrument (MSI). Sentinel-2 is a satellite developed under the European Space Agency's Environmental Monitoring and Security Program. Sentinel-2, a medium-resolution multispectral imaging satellite, equipped with a multispectral imager, has a total of 13 spectral bands, with spatial resolution ranging from 10 to 60 m and a revisit time of approximately 5 days for the same area. The bands utilized in this study, which have the highest spatial resolution (10 m), include blue ($\approx$465 nm), red ($\approx$665 nm), and near-infrared (NIR) ($\approx$842 nm). The data were acquired through the Google Earth Engine platform, using the collection "Harmonized Sentinel-2 MSI: MultiSpectral Instrument, Level-2A"(https://developers.google.com/earth-engine/datasets/catalog/COPERNICUS_S2_SR_HARMONIZED, accessed on 7 August 2024). Level-2A processing includes atmospheric correction, which eliminates atmospheric effects such as scattering and absorption by gases and aerosols, allowing for the recovery of surface reflectance values and ensuring consistent information for studies of terrestrial targets.

2.3. Development Stages of the Crop

SAR and optical images were obtained at three development stages of the soybean crop. These stages were selected based on the vegetative peak, determined by a time series based on the EVI (Figure 2b). The maximum value of the EVI coincides with the vegetative peak [6]. Moreover, this index is sensitive to dense vegetation, effectively reducing the atmospheric and soil background noise [26]. The three crop development stages of interest for image collection were:

- Stage 1: Between planting and the vegetative peak;
- Stage 2: During the vegetative peak;
- Stage 3: Between the vegetative peak and harvest.

SAR images were acquired on dates close to the optical images to minimize differences in the crops' phenological stages, with additional care taken to ensure no rainfall occurred during data collection, as the C-band can be affected by precipitation [4].

During the first development stage (Stage 1), the plants are just beginning to grow, and the radar (SAR) signal may be influenced by soil exposure, resulting in a low backscatter coefficient. Nevertheless, the type of soil also influences the SAR signal response, as well as soybean yield, potentially indicating a relationship between these factors. In the second development stage (Stage 2), when the crop reaches its vegetative peak and fully covers the area, the radar signal is influenced by the dense plant canopy. The backscatter coefficient tends to increase due to multiple scattering within the vegetation and between the vegetation and the soil. The density and structure of the canopy at this stage lead to a more complex interaction with radiation, increasing the SAR's sensitivity to biomass and vegetation water content. Additionally, the vegetative peak correlates well with the EVI vegetation index and soybean yield [27], suggesting that incorporating SAR data at this stage could enhance predictive performance. In the third development stage (Stage 3), the area is fully senescent, and both volume and moisture content begin to decrease. Despite this, the radar signal may still be influenced by the remaining plant structure. At this stage, SAR can detect changes in the texture and composition of senescent plants by interacting more with the dry branches and pods, which tends to correlate with the final crop yield. Figure 2a shows the similarity between EVI and *VV* and *VH* backscatter coefficient time-series.
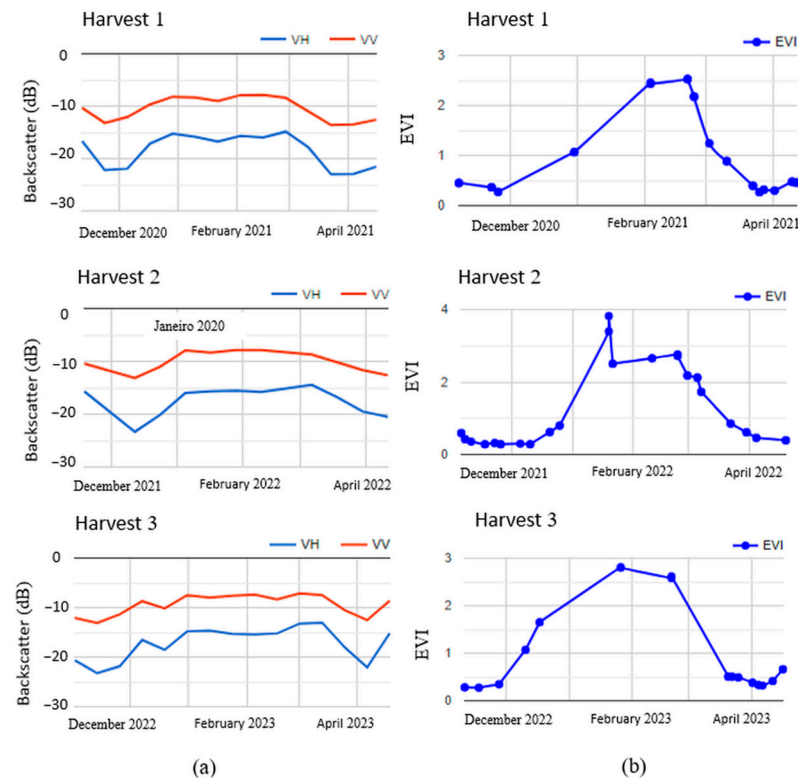
Figure 2. Temporal profiles of SAR data in *VV* and *VH* backscatter coefficient (**a**) and optical data considering EVI (**b**). The red circle represents the selected image dates based on the EVI.

2.4. Preprocessing of SAR Images

Initially, two types of preprocessing on the SAR images were performed: backscatter to obtain the backscatter coefficients (σ^0_{VV} and σ^0_{VH}) (Figure 3a) and polarimetric decomposition (angle α and entropy) (Figure 3b).

To obtain the *VH* and *VV* backscatter variables, the GRD data were processed following the method proposed by Filipponi [28]: (1) applying orbit files to obtain accurate satellite orbit and velocity vectors, ensuring proper georeferencing of the images; (2) thermal noise removal to eliminate thermal antenna noise affecting the images; (3) edge noise removal to eliminate noise at the edges of the images; and (4) radiometric calibration to normalize the amplitude observed in each band concerning the radar cross-section and obtain the backscattering coefficient (reflectivity per unit area) in $\beta0$ (a section necessary for performing radiometric terrain corrections). To reduce speckle noise, the Boxcar, Gamma, Lee, and Refined Lee filters available in the SNAP 10.0.0. software were evaluated using a filtering window of 3×3 to avoid loss of detail [13]. Terrain correction was performed using the digital elevation model (DEM) with a spatial resolution of 12.5 m from the Palsar sensor (https://search.asf.alaska.edu/, accessed on 20 June 2024), transformed to the UTM—23S coordinate system, datum WGS84. Finally, the backscatter coefficient was converted to dB using a logarithmic transformation.

For the second processing, SLC data were used to perform polarimetric decomposition and generate the Entropy and Alpha variables. With these data, we first performed the split to select a subset and lighten the processing load. Next, we applied the orbit file to improve accuracy, as described in the GRD data. After that, we conducted a deburst to remove the bursts inherent to these images. The covariance matrix C2 was calculated, followed by the Cloude and Pottier polarimetric decomposition for dual-polarization data, generating Entropy (H) and Alpha. Multilooking was also applied to these images to regularize the pixels [29], using a 4 (range) × 1 (azimuth) window, resulting in an image with a spatial resolution of 14.05 m [30]. Finally, terrain correction was applied in the same manner as for the GRD data.
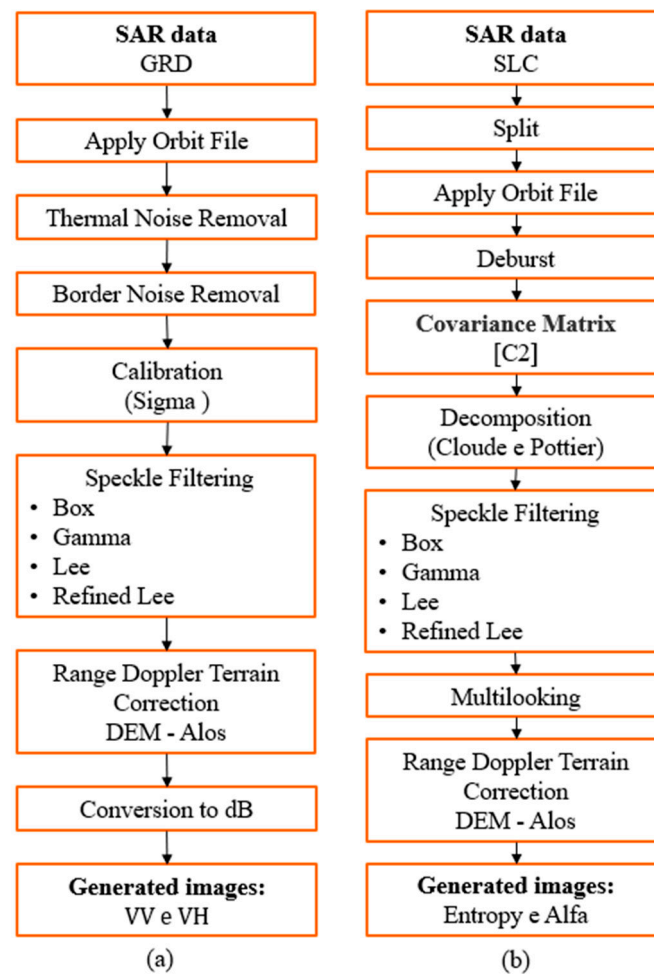
Figure 3. SAR data workflow for obtaining (**a**) backscatter coefficients and (**b**) polarimetric decomposition.

Speckle Noise Filters

This study evaluated the most mentioned filters in the literature, namely Boxcar, Lee, Gamma, and Refined Lee (Table 1). The Boxcar filter calculates the average value of a window centered on each pixel to homogenize the image based on the surrounding pixels [31]. The Lee filter assumes that the intensity of the image at each pixel follows a local Gaussian distribution, which allows for speckle noise reduction without significant loss of detail [32]. The Gamma filter focuses on minimizing texture information loss by using the coefficient of variation (CV) and contrast ratios, with theoretical probability density functions determining the smoothing process [33]. The Refined Lee filter is an enhancement of the Lee filter, capable of preserving textural features, which is important for detecting crops, soils, and other terrain characteristics [34].

Therefore, at the end of the image preprocessing, 16 SAR images were obtained for each development stage: 8 from the backscatter coefficient data (considering the two polarizations *VH* and *VV*, with 4 different filters) and 8 images from the polarimetric decomposition (Alpha and entropy, using the 4 tested filters).

Table 1. List of tested filters and their mathematical approaches.

Filter	Equation	In Which:
Boxcar	$\frac{1}{N}\sum_{p=1}^{N} I_{(p,q)}$	N is the number of pixels in the neighborhood, and $I_{(p,q)}$ are the pixel values in the neighborhood.

Table 1. *Cont.*

Filter	Equation	In Which:
Lee	$I(i,j) + \frac{\sigma^2}{\sigma^2 + Var(N)}[Mean(N) - I(i,j)]$	σ^2 is the global variance of the image, $Var(N)$ is the local variance in the neighborhood, and $Mean(N)$ is the local mean in the neighborhood.
Gamma	$\frac{\sum_{p=1}^{N} \omega(p) \times (p,q)}{\sum_{P=1}^{N} \omega(p)}$	$\omega(p)$ weights are the values assigned to the pixels in the neighborhood
Refined Lee	$I(i,j) + \frac{\propto \times \sigma^2}{\sigma^2 + Var(N)}$	$\propto$ is an adjustment factor.

2.5. Variables

From these data, four SAR-derived vegetation indices were calculated from the backscatter coefficients: DPSVI, RFDI, Pol, and RVI. Additionally, EVI was calculated using optical data (Table 2). The EVI was used based on studies by [6,35], which demonstrated that using this index in machine learning algorithms can assist in soybean yield prediction.

Table 2. Equations of the SAR and EVI vegetation indices used.

Index	Equation	Reference
DPSVI	$\frac{VV^2 + VV \times VH}{\sqrt{2}}$	[36]
RFDI	$\frac{VV - VH}{VV + VH}$	[37]
Pol	$\frac{VH - VV}{VH + VV}$	[38]
RVI	$\frac{4 \times \sigma_{VV}^0}{\sigma_{VV}^0 + \sigma_{VH}^0}$	[39]
EVI	$\frac{2.5(NIR - R)}{(NIR + 6R - 7.5B + 1)}$	[40]

Therefore, for this study, eight variables were generated from SAR data (Alpha, Entropy, DPSVI, RFDI, Pol, RVI, *VH*, and *VV*), in addition to the EVI. For the SAR data, each of these variables was evaluated using the four different speckle noise filters. All SAR variables and EVI were obtained for the three development stages of the crop and for the three tested growing harvests. After obtaining all the images, a 15 m buffer was applied along the field boundaries to crop the images, with the aim of eliminating the influence of uncultivated areas in the pixels.

2.6. Correlation

To correlate yield values with the imagery outputs, the pixels from the input images were extracted to match the coordinates of the yield data. From these data, we selected 15,000 points per growing harvest by a randomization process to continue the procedures, aiming to optimize data analysis and processing. This random selection maintained the frequency distribution of the data as well as the measures of central tendency and dispersion (Table 3). Thus, the selection did not compromise the results but facilitated the entire modeling and analysis process. Since the data often did not follow a normal distribution, we used Spearman's correlation.

Table 3. Descriptive statistics of the full datasets in each area (after cleaning) and the 15,000 randomly selected yield points. Data in tons per hectare.

Statistics	Harvest 1		Harvest 2		Harvest 3	
	Full Data	15 k Points	Full Data	15 k Points	Full Data	15 k Points
Mean	3.50	3.51	2.97	2.97	5.08	5.08
Median	3.44	3.44	2.99	2.99	5.05	5.05
Standard deviation	0.77	0.78	0.86	0.86	0.72	0.72
CV%	22.20	22.23	28.98	29.14	14.20	14.14
Minimum value	1.14	1.18	1.01	1.04	2.84	3.00
Maximum value	5.95	5.86	5.47	5.46	7.93	7.93
Q1	2.93	2.93	2.38	2.38	4.58	4.58
Q3	4.04	4.05	3.53	3.54	5.54	5.55
Interquartile range	1.11	1.11	1.14	1.16	0.95	0.96
n	71,832	15,000	59,141	15,000	59,568	15,000

2.7. Predictions

Based on the correlation between SAR variables and their different speckle filters and yield, the speckle filter that provided the best performance to do the predictions was chosen. Additionally, when correlating the SAR variables, those with correlations higher than 80% among themselves were discarded to avoid collinearity issues in the prediction models. From there, predictions using only the selected filter and the SAR variables with the lowest correlations among themselves were carried out, which could result in complementary information.

Random Forest (RF) was the machine learning algorithm used in this study to estimate soybean yield, due to its robustness and widespread use in yield predictions. For this, the set of 15,000 yield data points for each harvest was randomly divided into 70% for training and 30% for testing. The parameters used for the regressions were the default settings of the algorithm: nodesize = 5, mtry = p/3, where p is the number of predictors, with the only modification being the number of trees (ntree) reduced from 500 to 150 for reducing operational costs. The RF models were evaluated using the coefficient of determination (R^2) and the root mean squared error (RMSE) for the testing set as error metrics.

For the predictions, models were evaluated exclusively with the optical vegetation index (using only EVI) and models including EVI and SAR variables (Figure 4), to understand whether SAR variables improve the performance of soybean yield prediction. Initially, a scenario was evaluated including all SAR variables and EVI from the three development stages together, compared to using only EVI at all three stages (Figure 4a). Subsequently, models were created using all SAR variables for each of the three stages separately, to determine if including SAR variables at separate stages optimizes performance and which stage is better for predicting soybean yield (Figure 4b). Using the growing stage that showed the best performance, models were evaluated with each SAR variable and EVI separately to evaluate the performance of each individual SAR variable and further optimize predictions (Figure 4c). This process led to the identification of the stage and SAR variable that provided the best performance for soybean yield prediction.
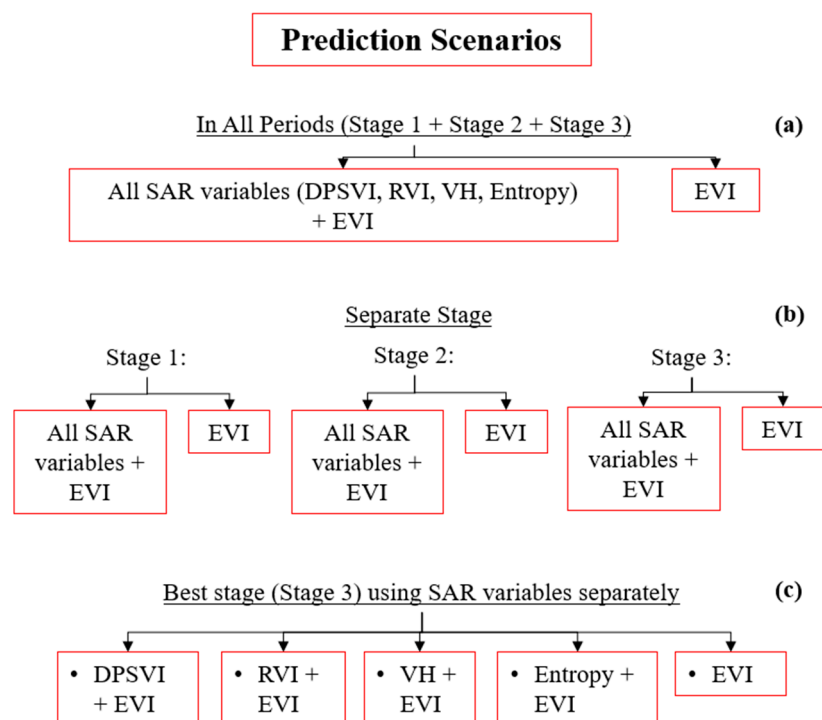
Figure 4. Prediction scenarios performed. Input data corresponding to each tested scenario (in red): (**a**) using all stages and SAR variables together, (**b**) using stages separately and all SAR variables together, (**c**) using the stage that previously performed best with the variables separated.

3. Results and Discussion

3.1. Correlation Between Remote Sensing Data and Yield

In general, the SAR images did not show a direct relationship with soybean yield in any of the three growth stages, analyzed filters, or SAR variables (Figure 5). The correlation results were frequently low, remaining below ±0.35. This low association might be attributed to the SAR image parameters, which are influenced by structural factors of the crop, such as leaf area, biomass, and canopy height [14], aspects that may not have a direct relation to soybean grain yield. Although planting density was consistent across the three harvests and the cultivars had an indeterminate growth habit, factors that would affect SAR signal response, no evident pattern was found between growth stages, vegetation indices, and crop harvest in the correlations. Yield predictions using remote sensing rely on the direct relationship between vegetation indices and biomass, and the relationship between biomass and yield [3]. However, the number of pods per plant is the primary determinant of grain yield [41], and there can be significant variation in biomass and pod and grain formation, where higher biomass does not always result in higher yields. Additionally, the correlation between EVI and yield (Table 4) did not exceed 0.5, indicating that soybean shows a low correlation with optical remote sensing data, even when using other vegetation indices [35]. The negative correlations of EVI observed during growth stages 1 and 2 for harvest 3 and stage 3 for harvest 2 might indicate the presence of weeds [42]. Remote sensing data are influenced not only by the cultivated plants but also by weeds in the area. The interference from these weeds can distort the relationship between vegetative biomass and yield, as they compete for resources and can reduce the yield of the main crop while still reflecting a high EVI and distorting SAR data. Another factor to note is that filter patterns are very similar within the same harvest, indicating that there are no consistent variations in correlation with soybean yield when using different speckle noise filters.
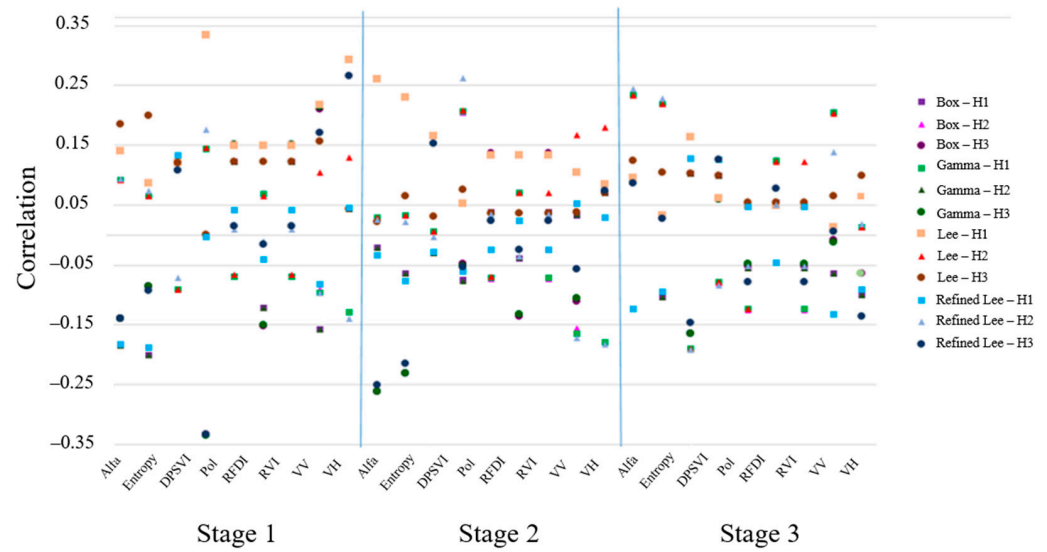
Figure 5. Spearman correlation coefficient between SAR data and soybean yield, including harvest, growth stages, speckle noise reduction filters, and SAR variables. Significant correlations at 5%.

Table 4. Spearman correlation coefficient between EVI values and yield data at the three different growth stages and three harvests. Significant correlations at 5%.

	Harvest 1	Harvest 2	Harvest 3
Stage 1	0.27	0.51	−0.34
Stage 2	0.41	0.50	−0.17
Stage 3	0.54	−0.25	0.14

3.2. Speckle Filter Correlation with Soybean Yield

When statistically examining the filters for the *VH* index from the first harvest it is evident that the Refined Lee filter stands out as the most divergent compared to the other filters, as also shown in the correlation between filters (Table 5). The Refined Lee filter introduces scattered black pixels into the images, making them noisier. Although statistically robust, studies by [43] comparing the effectiveness of speckle noise filters demonstrated that the Refined Lee filter is more effective for detecting small, distinct features, making it less suitable for homogeneous crop cover. Therefore, for studies focused on crop yield, particularly in soybean fields where the vegetation cover is uniform and lacks sharp variations, the Refined Lee filter is not the optimal choice.

When correlating pixel values using *VH* across the development stages among the speckle noise filters, significant similarities were observed between the filtering algorithms. The Boxcar, Gamma, and Lee filters show correlations close to 1, suggesting no significant distinction in their effects on yield relationships (Table 5). This high correlation between Gamma, Lee, and Boxcar filters may be attributed to their adaptive nature, relying on different methods of local pixel distribution within the window, thus preserving image edges [44]. Nevertheless, in crops such as soybean, which present a homogeneous appearance with few abrupt variations, the influence of the filters is not significant in the analyses. Therefore, as there are no significant differences in choosing between these filters, the study proceeded with the Boxcar filter, since it is the simplest mathematically among the others [45] and is commonly used in agricultural studies [23,46].

Table 5. Spearman correlation coefficient between the tested filters based on *VH* polarization backscatter coefficient values combined with SAR images across the three growing harvests and three development stages. Significant correlations at 5%.

	Boxcar	Gamma	Lee	Refined Lee
Harvest 1				
	Boxcar	Gamma	Lee	Refined Lee
Boxcar	1	-	-	-
Gamma	0.999	1	-	-
Lee	0.999	0.999	1	-
Refined	0.914	0.907	0.911	1
Harvest 2				
	Boxcar	Gamma	Lee	Refined Lee
Boxcar	1	-	-	-
Gamma	0.999	1	-	-
Lee	0.999	0.999	1	-
Refined	0.914	0.911	0.913	1
Harvest 3				
	Boxcar	Gamma	Lee	Refined Lee
Boxcar	1	-	-	-
Gamma	0.999	1	-	-
Lee	1	0.999	1	-
Refined	0.830	0.907	0.911	1

3.3. Correlation of SAR Variables with Soybean Yield

When correlating SAR variables derived from the processing of backscatter coefficients (DPSVI, RFDI, RVI, Pol, *VH*, and *VV*), we observed some indices with correlations equal to 1 and others below 0.2. With *VV*, except in the third development stage of the first growing harvest (Table 6), the correlations with DPSVI, RFDI, RVI, and Pol were above 0.8, while *VH* correlations did not exceed 0.6. Additionally, studies by Le Toan et al. [47] and McNair et al. [48] show that *VH* works better when plants do not grow straight up, such as maize, and are not affected by the direction the rows are planted. Given that soybean is an herbaceous plant, *VH* is more suitable than *VV* for this type of crop, and *VH* showed a lower correlation with other SAR variables, while its correlation with yield remained within a similar range to *VV*. The SAR vegetation indices (RFDI, Pol, and RVI) showed an almost perfect correlation (r ~ 1), whereas with DPSVI, the correlation was frequently below 0.70. The RFDI, Pol, and RVI indices were developed for monitoring plant growth, crop classification, and land use but were not initially designed for agricultural applications [41,47,49,50]. Thus, they may lack sensitivity to identify variability within the same agricultural crop.

Table 6. Spearman correlation coefficient between SAR variables and vegetation indices derived from backscatter coefficients. Significant correlations at 5%.

Harvest 1—Stage 1						Harvest 2—Stage 1					
DPSVI	−0.71	0.71	−0.71	−0.22	−0.97	DPSVI	−0.72	0.72	−0.72	−0.35	−0.97
-	Pol	−1	1	−0.47	0.86	-	Pol	−1	1	−0.36	0.86
-	-	RFDI	−1	0.47	−0.86	-	-	RFDI	−1	0.36	−0.86
-	-	-	RVI	−0.47	0.86	-	-	-	RVI	−0.36	0.86
-	-	-	-	*VH*	0.021	-	-	-	-	*VH*	0.13
-	-	-	-	-	*VV*	-	-	-	-	-	*VV*

Table 6. *Cont.*

Harvest 1—Stage 2					
DPSVI	−0.67	0.67	−0.67	0.31	−0.96
-	Pol	−1	1	−0.45	0.83
-	-	RFDI	−1	0.45	−0.83
-	-	-	RVI	−0.45	0.83
-	-	-	-	*VH*	0.001
-	-	-	-	-	*VV*

Harvest 2—Stage 2					
DPSVI	−0.68	0.68	−0.68	0.22	−0.96
-	Pol	−1	1	−0.51	0.85
-	-	RFDI	−1	0.51	−0.85
-	-	-	RVI	−0.51	0.85
-	-	-	-	*VH*	0.033
-	-	-	-	-	*VV*

Harvest 1—Stage 3					
DPSVI	−0.58	0.58	−0.58	−0.43	−0.97
-	Pol	−1	1	−0.42	0.76
-	-	RFDI	−1	0.42	−0.76
-	-	-	RVI	−0.42	0.76
-	-	-	-	*VH*	0.21
-	-	-	-	-	*VV*

Harvest 2—Stage 3					
DPSVI	−0.62	0.62	−0.62	−0.29	−0.96
-	Pol	−1	1	−0.52	0.80
-	-	RFDI	−1	0.52	−0.80
-	-	-	RVI	−0.52	0.80
-	-	-	-	*VH*	0.039
-	-	-	-	-	*VV*

Harvest 3—Stage 1					
DPSVI	−0.63	0.63	−0.63	−0.36	−0.96
-	Pol	−1	1	−0.45	0.81
-	-	RFDI	−1	0.45	−0.81
-	-	-	RVI	−0.45	0.81
-	-	-	-	*VH*	0.12
-	-	-	-	-	*VV*

Harvest 3—Stage 3					
DPSVI	−0.61	0.61	−0.61	−0.32	−0.95
-	Pol	−1	1	−0.47	0.80
-	-	RFDI	−1	0.47	−0.80
-	-	-	RVI	−0.47	0.80
-	-	-	-	*VH*	0.11
-	-	-	-	-	*VV*

Harvest 3—Stage 2					
DPSVI	−0.68	0.68	−0.68	0.25	−0.97
-	Pol	−1	1	−0.41	0.83
-	-	RFDI	−1	0.41	−0.83
-	-	-	RV	−0.41	0.83
-	-	-	-	*VH*	0.12
-	-	-	-	-	*VV*

For the variables generated from polarimetric decomposition (alpha and entropy), both showed a high correlation with each other (r > 0.85—Table 7) across all development stages of the crop. Entropy reflects the disorder of the reflected energy from a target, and for soybeans, its value increases as the crop develops (Figure 2), indicating the presence of multiple scattering events, which is expected in a crop canopy [14]. Therefore, entropy is more appropriate in this context, as it better captures variations in crop growth over time [51] and is not affected by the direction in which the rows are planted.

Table 7. Correlation between variables derived from polarimetric decomposition.

	Stage 1	**Stage 2**	**Stage 3**
Harvest 1	0.90	0.90	0.93
Harvest 2	0.86	0.88	0.87
Harvest 3	0.93	0.91	0.90

To complement the information within a prediction algorithm, SAR variables with less than 80% correlation with each other were used. This approach improves prediction performance by including non-collinear variables in a predictive model [52]. Among the backscatter-related variables, DPSVI, RVI, and *VH* were selected due to their lower correlations with each other (Table 6), providing complementary information for the prediction scenarios. Regarding the variables from polarimetric decomposition, alpha was excluded, and only entropy was used. Thus, for the prediction scenarios, the selected SAR variables were DPSVI, RVI, *VH*, entropy, and EVI across the three stages, using the Boxcar filter

3.4. Predictions

3.4.1. Considering All Stages Together

Initially, the scenario using only SAR data was not viable due to the low correlations with soybean yield (Figure 5). Using scenarios with data from all growth stages, the integration of EVI and all SAR variables showed superior performance in predicting soybean yield compared to the model using only EVI (Figure 6). However, this improvement in prediction performance was less than 2% in terms of R^2 and 3% in RMSE, not exceeding the second decimal place (Table 8). Despite the observed improvement by including SAR indices, the high computational cost associated with processing SAR images must be considered. When optical images are available for all three development stages of soybean, the performance using only these optical images is like the performance with the inclusion of SAR. Therefore, if optical images are available for all three stages, it is more economical and efficient to use only these optical images rather than incorporating SAR data.
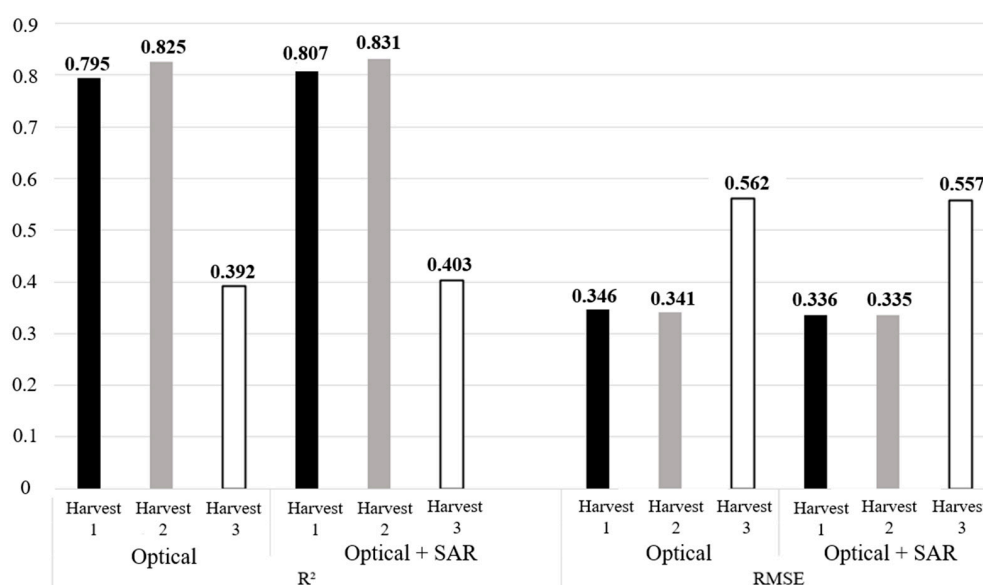
Figure 6. R^2 and RMSE values of predictions for each harvest individually with all stages of image collection, using only optical data (EVI) compared to using optical data together with all SAR variables.

Table 8. Percentage difference in performance of R^2 and RMSE when comparing scenarios that include SAR data from all stages across different harvests with scenarios using SAR and EVI, versus using only EVI.

	Difference in %	
	R^2	RMSE
Harvest 1	1.51	−2.89
Harvest 2	0.73	−1.76
Harvest 3	2.81	−0.89

Observing the harvests, there was a difference in prediction performance for harvest 3 compared to the other harvests. This can be seen in the actual yield maps (Figure 1), where there were significant spatial differences as well as differences in yield values. In the first and second harvests, the most productive area is concentrated in the south, while in the third harvest, this pattern is reversed. Additionally, the change in cultivars in harvest 3 compared to harvests 1 and 2 may have affected the SAR sensor's response: in harvest 3, a mix of cultivars was used, one of which has a high tendency for branching, unlike the other harvests. This high branching alters the plant's structure in terms of leaf density, leaf and branch arrangement, and moisture, which directly influences how radar

electromagnetic energy interacts with the target [13,14]. This can be observed in Figure 7, where different patterns in DPSVI are noticeable, especially in stage 3 of harvest 3 in the area with different cultivars.
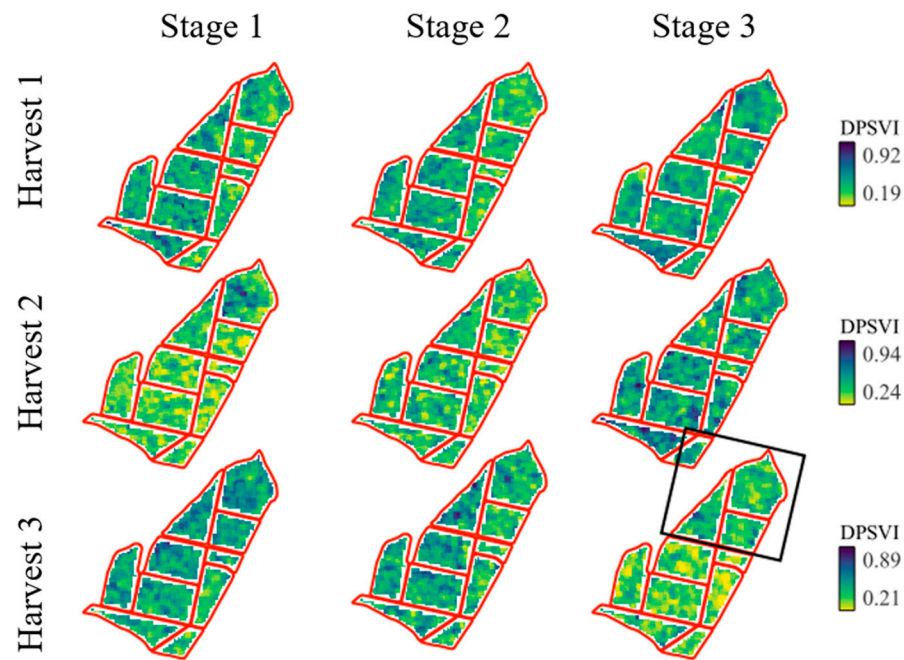

Figure 7. DPSVI index map for distinct growth stages and soybean harvests. The highlighted area in black shows the difference in cultivar in harvest 3.

3.4.2. Predictions by Separating Stages

When predictions were made by separating the stages and including SAR variables (DPSVI, RVI, *VH*, and entropy) along with EVI, better R^2 values (Figure 8) and RMSE values (Figure 9) were achieved compared to using all three stages together with both SAR and optical data. Moreover, separating the stages showed that the performance of predictions including SAR variables alongside EVI surpassed that of using EVI alone, resulting in increases ranging from 6% to 18% in R^2 values between the stages.
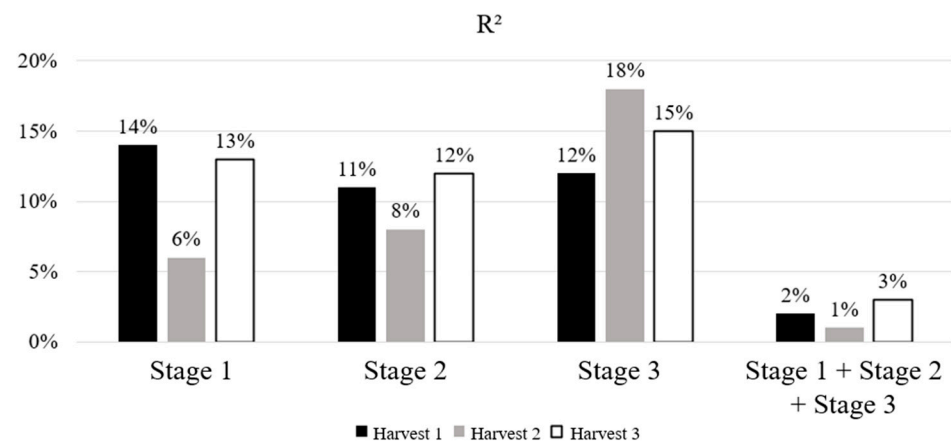
Figure 8. Percentage difference in R^2 of predictions with EVI and adding SAR variables in models using each stage individually compared to all stages combined.
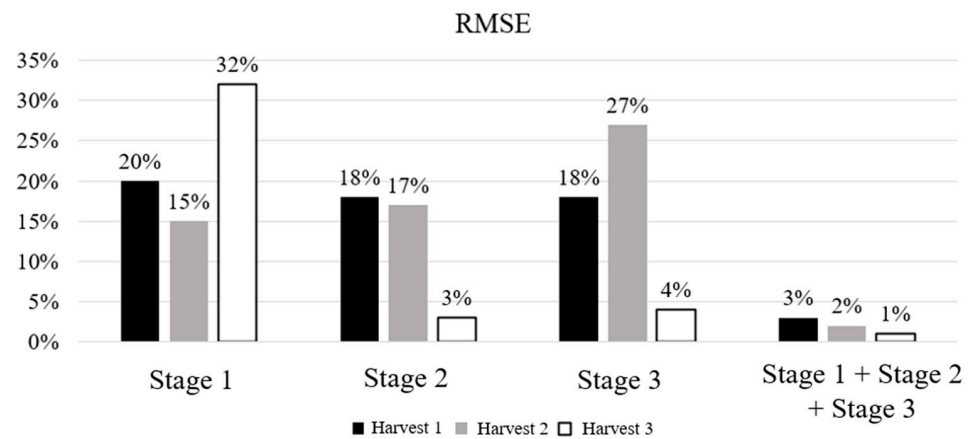
Figure 9. Percentage difference in RMSE of predictions with EVI and adding SAR variables in models using each stage individually compared to all stages combined.

Improved performance was observed when incorporating SAR data and separating the analysis by development stages, resulting in higher coefficients of determination (R^2) and lower RMSE compared to using optical data alone (Figures 10 and 11; Table 9). In Stage 1, the plants had not reached their full growth stage, with greater influence from soil moisture or crop residue [53]. Similar effects of soil on backscattering response in the initial stages of vegetative development are also reported by Cable et al. [54] and Mandal et al. [41]. In Stage 2, when the crop reaches peak vegetative growth, backscatter is primarily determined by the scattering from the upper leaf layer [55], resulting in volumetric backscatter due to the dense leaf cover. At this stage, the crop retains most moisture in the leaves, which increases backscatter and interferes more with the radar signal [56]. Conversely, signal saturation can occur due to the high canopy density of SAR and optical images [57]. Therefore, at this stage, the radar signal is influenced by moisture and interaction with canopy biomass, which does not relate directly to grain yield. In Stage 3, with plants in the maturation phase and reduced leaf area, adding information from SAR data during this phase considers the radar wave's greater ability to penetrate moderately dry canopies, as variations in vegetation water content can reduce SAR signal attenuation [58]. Thus, the inclusion of SAR data in Stage 3 showed the most significant improvement compared to the other stages when using only optical data, making it the best option for including SAR data to enhance soybean yield predictions. This result highlights the ability of SAR data to provide complementary information to that obtained from optical sensors [12], especially when the availability of optical images before and during peak vegetative growth is more challenging due to high cloud cover.
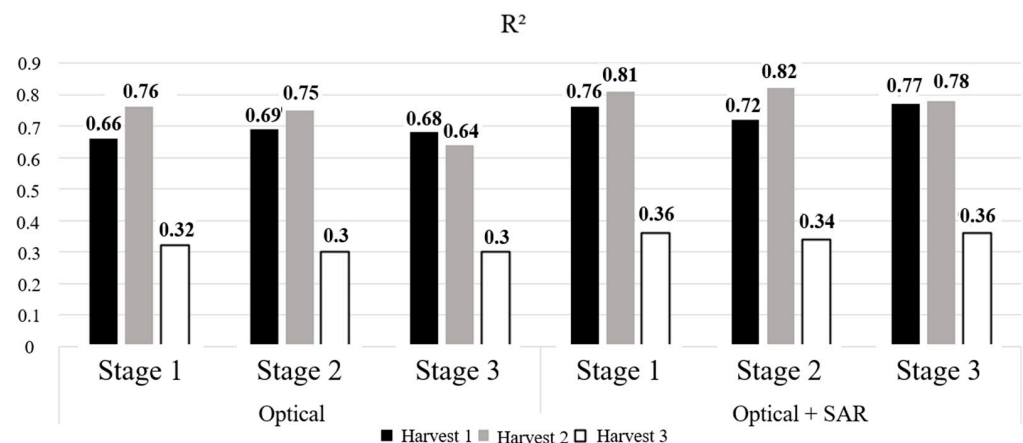

Figure 10. R^2 values for predictions using all growth stages with only optical data and using optical data in conjunction with all SAR variables.
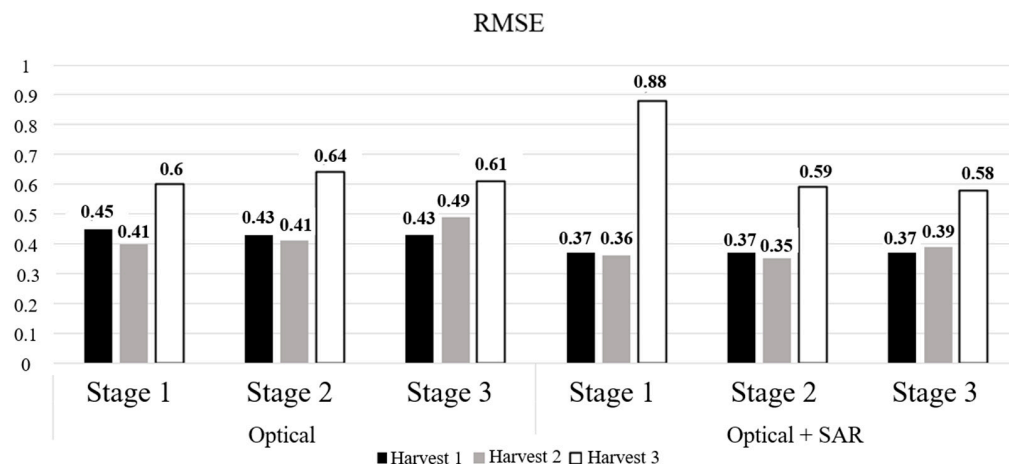
Figure 11. RMSE values for predictions using all growth stages with only optical data and using optical data in conjunction with all SAR variables.

Table 9. Difference (%) of tested scenarios using SAR + optical data compared to optical data only in separate stages.

	Difference in %					
	Stage 1		**Stage 2**		**Stage 3**	
	R^2	**RMSE**	R^2	**RMSE**	R^2	**RMSE**
Harvest 1	14%	−20%	11%	−18%	12%	−18%
Harvest 2	6%	−14%	8%	−17%	18%	−27%
Harvest 3	13%	32%	12%	−3%	15%	−4%

3.4.3. The Best Growth Stage for Yield Prediction

When using scenarios with each SAR variable individually in conjunction with EVI for stage 3, a maximum difference of 18% was obtained compared to the scenario that included all SAR variables for stage 3 (Figure 12, Table 10). Utilizing only one SAR variable reduces operational costs and makes the modeling process more efficient compared to using all SAR variables combined with EVI. Moreover, for harvest 3, we achieved better results by including only one SAR variable in the model along with EVI, specifically the models used DPSVI, RVI, *VH*, and entropy separately with EVI. Among these variables, the advantage of using DPSVI is greater, as it is derived from backscatter data and is available in GRD data. Additionally, the predicted yield maps using this configuration showed a good visual correlation with the actual yield maps (Figure 13). The prediction error map, which compares predicted yield with actual yield, shows higher occurrences of errors at the field boundaries (Figure 13).

Table 10. Percentage difference between scenarios using only one SAR index + EVI compared to the scenario using all SAR variables combined with EVI at Stage 3.

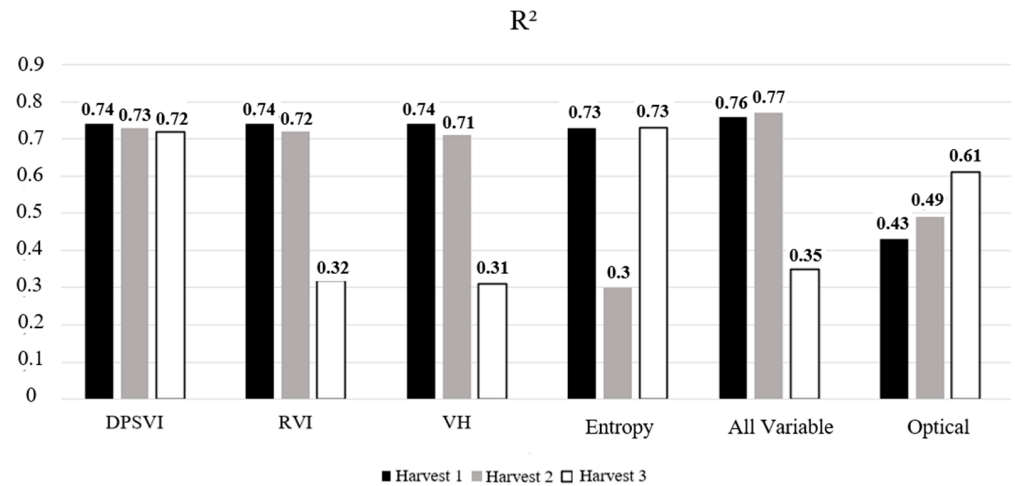|	Stage 3—Difference (%)							
	DPSVI		**RVI**		*VH*		**Entropy**	
	R^2	**RMSE**	R^2	**RMSE**	R^2	**RMSE**	R^2	**RMSE**
Harvest 1	−4%	6%	−4%	−49%	−3%	5%	−4%	6%
Harvest 2	−18%	27%	−6%	−37%	−8%	14%	−18%	27%
Harvest 3	104%	−27%	−8%	19%	−11%	3%	106%	−28%

Figure 12. R^2 values obtained for Stage 3 using scenarios with separate SAR variables in conjunction with EVI, compared to using all SAR variables combined with EVI and using only optical data (EVI).
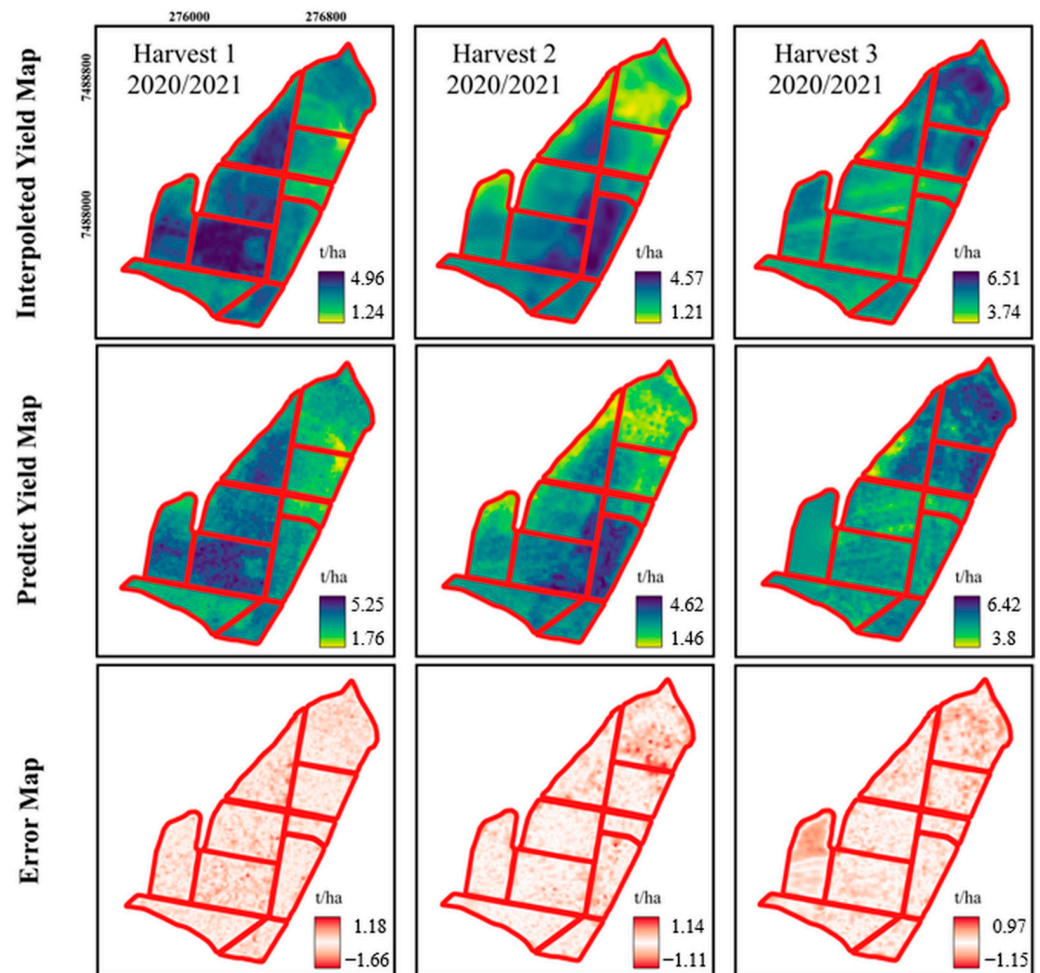

Figure 13. Visual comparison between actual yield maps and predicted yield using DPSVI in conjunction with EVI for Stage 3, using the Boxcar filter. The actual yield data were interpolated using ordinary kriging. The error maps represent the difference between the actual and predicted maps, showing positive and negative variations.

Although SAR data can enhance soybean yield predictions, there are some limitations that may impact their implementation. Processing SAR data requires specialized knowledge, as they provide information with different processing levels compared to

optical sensors. Furthermore, the inherent noise in SAR images can influence the accuracy of predictions, especially in areas with homogeneous vegetation cover, such as soybean fields [59,60]. When compared with previous studies, such as Hosseni [23], which utilized only entropy and alpha data, we observed that by employing a different polarimetric decomposition method and a distinct deep learning algorithm, their prediction accuracy surpassed ours (R^2: Hosseni: 0.81 and ours: 0.76). However, the complexity and high computational costs of these approaches make their implementation less viable for end users. The Random Forest regression algorithm stands out for its ability to handle large datasets, resulting in accurate predictions with lower computational costs than deep learning algorithms. This makes it a popular choice for yield prediction in agricultural scenarios. Additionally, simpler regression algorithms can be adapted for use with SAR data and have the potential to further enhance prediction accuracy in field-scale agricultural areas. Therefore, it is essential for future research to address these limitations to strengthen the validity and applicability of findings in precision agriculture.

4. Conclusions

SAR images do not show a direct correlation with soybean yield; thus, using SAR data alone is not yet a viable alternative for predicting soybean yield within the fields in a harvest when optical data is not available.

The filters evaluated for reducing speckle noise revealed that the Refined Lee filter performed the worst compared to the others. However, evaluating the different filters did not result in significant improvements in the correlation with yield. Therefore, choosing the Boxcar filter is advantageous, since it has the lowest operational cost among all the tested options.

Testing prediction scenarios that include SAR data alongside EVI showed improved performance. Nonetheless, this difference was minimal in some situations (3–49%), but the computational effort required to process SAR data must be considered.

Using only the DPSVI index and EVI after the vegetative peak resulted in superior predictive performance compared to other stages or SAR variables, compared to the use of optical data alone. This finding underscores the potential of SAR data to significantly improve the accuracy of yield predictions. SAR data offers valuable complementary insights that enhance those obtained from optical sensors, particularly in scenarios where acquiring optical images before and during peak vegetative growth is difficult due to high cloud cover.

Given that soybean yield does not correlate well with remote sensing data, further studies with other crops may provide better predictive results using SAR imagery for yield estimation. It is important to consider conducting experiments in more areas and testing different cultivars to obtain a more comprehensive and accurate understanding of the potential of SAR images in predicting soybean yield.

Author Contributions: Conceptualization, I.A.C. and L.R.A.; methodology, I.A.C., G.M.M.B. and L.R.A.; validation, V.H.R.P. and G.M.M.B.; formal analysis, I.A.C.; investigation, I.A.C.; resources, L.R.A.; data curation, I.A.C. and D.D.M.; writing—original draft preparation, I.A.C. and D.D.M.; writing—review and editing, I.A.C., G.M.M.B., V.H.R.P., D.D.M. and L.R.A.; visualization, L.R.A.; supervision, L.R.A. and G.M.M.B.; project administration, L.R.A. All authors have read and agreed to the published version of the manuscript.

Institutional Review Board Statement: Not applicable.

Data Availability Statement: The data presented in this study are available on request from the corresponding author. The data are not publicly available due to privacy concerns regarding yield data.

References

1. Van Ittersum, M.K.; Cassman, K.G.; Grassini, P.; Wolf, J.; Tittonell, P.; Hochman, Z. Yield gap analysis with local to global relevance—A review. *Field Crops Res.* **2013**, *143*, 4–17. [CrossRef]
2. Jin, X.; Kumar, L.; Li, Z.; Feng, H.; Xu, X.; Yang, G.; Wang, J. A review of data assimilation of remote sensing and crop models. *Eur. J. Agron.* **2018**, *92*, 141–152. [CrossRef]
3. Delécolle, R.; Maas, S.J.; Guerif, M.; Baret, F. Remote sensing and crop production models: Present trends. *ISPRS J. Photogramm. Remote Sens.* **1992**, *47*, 145–161. [CrossRef]
4. Jensen, J.R. *Sensoriamento Remoto: Uma Perspectiva em Recursos Terrestres*, 2nd ed.; Parêntese: São José dos Campos, Brazil, 2009.
5. Fountas, S.; Espejo-García, B.; Kasimati, A.; Mylonas, N.; Darra, N. O futuro da agricultura digital: Tecnologias e oportunidades. *IT Prof.* **2020**, *22*, 24–28. [CrossRef]
6. Richetti, J.; Judge, J.; Boote, K.J.; Johann, J.A.; Uribe-Opazo, M.A.; Becker, W.R.; Paludo, A.; Silva, L.C.A. Using phenology-based enhanced vegetation index and machine learning for soybean yield estimation in Paraná State, Brazil. *J. Appl. Remote Sens.* **2018**, *12*, 026029. [CrossRef]
7. You, J.; Li, X.; Low, M.; Lobell, D.; Ermon, S. Deep Gaussian Process for Crop Yield Prediction Based on Remote Sensing Data. In Proceedings of the AAAI Conference on Artificial Intelligence, San Francisco, CA, USA, 1–9 February 2017; Volume 31, p. 1.
8. Dalla Betta, M.M.; Trabaquini, K.; Elias, H.T.; Silva, M.S. Mapeamento da soja por meio de imagens Landsat e Sentinel-2 nos municípios de Lages e Capão Alto em Santa Catarina. *Agropecuária Catarin.* **2022**, *35*, 68–73. [CrossRef]
9. Silveira, H.L.F.; Eberhardt, I.D.R.; Sanches, I.D.A.; Galvão, L.S. Análise da Cobertura de Nuvens No Nordeste Do Brasil e Seus Impactos No Sensoriamento Remoto Agrícola Operacional. Simpósio Brasileiro de Sensoriamento Remoto. 2017. Available online: https://www.alice.cnptia.embrapa.br/alice/handle/doc/1074562 (accessed on 26 September 2024).
10. Eberhardt, I.D.R.; Schultz, B.; Rizzi, R.; Sanches, I.D.A.; Formaggio, A.R.; Atzberger, C.; Barreto Luiz, A.J. Cloud cover assessment for operational crop monitoring systems in tropical areas. *Remote Sens.* **2016**, *8*, 219. [CrossRef]
11. Prudente, V.H.R.; Martins, V.S.; Vieira, D.C.; Silva, N.R.D.F.; Adami, M.; Sanches, I.D.A. Limitations of cloud cover for optical remote sensing of agricultural areas across South America. *Remote Sens. Appl. Soc. Environ.* **2020**, *20*, 100414. [CrossRef]
12. Bahrami, H.; Homayouni, S.; Safari, A.; Mirzaei, S.; Mahdianpari, M.; Reisi-Gahrouei, O. Deep learning-based estimation of crop biophysical parameters using multi-source and multi-temporal remote sensing observations. *Agronomy* **2021**, *11*, 1363. [CrossRef]
13. Nasirzadehdizaji, R.; Balik Sanli, F.; Abdikan, S.; Cakir, Z.; Sekertekin, A.; Ustuner, M. Sensitivity analysis of multi-temporal Sentinel-1 SAR parameters to crop height and canopy coverage. *Appl. Sci.* **2019**, *9*, 655. [CrossRef]
14. McNairn, H.; Shang, J. A review of multitemporal synthetic aperture radar (SAR) for crop monitoring. In *Multitemporal Remote Sensing: Methods and Applications*; Ban, Y., Ed.; Springer: New York, NY, USA, 2016; pp. 317–340.
15. Schlund, M.; Erasmi, S. Sentinel-1 time series data for monitoring the phenology of winter wheat. *Remote Sens. Environ.* **2020**, *246*, 111814. [CrossRef]
16. Prudente, V.H.R.; Oldoni, L.V.; Vieira, D.C.; Cattani, C.E.V.; Sanches, I.D. Relationship between SAR/Sentinel-1 polarimetric and interferometric data with biophysical parameters of agricultural crops. *Int. Arch. Photogramm. Remote Sens. Spat. Inf. Sci.* **2019**, *42*, 599–607. [CrossRef]
17. Mestre-Quereda, A.; Lopez-Sanchez, J.M.; Vicente-Guijalba, F.; Jacob, A.W.; Engdahl, M.E. Time-series of Sentinel-1 interferometric coherence and backscatter for crop-type mapping. *IEEE J. Sel. Top. Appl. Earth Obs. Remote Sens.* **2020**, *13*, 4070–4084. [CrossRef]
18. Mandal, D.; Kumar, V.; Ratha, D.; Dey, S.; Bhattacharya, A.; Lopez-Sanchez, J.M.; McNairn, H.; Rao, Y.S. Dual polarimetric radar vegetation index for crop growth monitoring using Sentinel-1 SAR data. *Remote Sens. Environ.* **2020**, *247*, 111954. [CrossRef]
19. Yommy, A.S.; Liu, R.; Wu, S. SAR image despeckling using refined Lee filter. In Proceedings of the 2015 7th International Conference on Intelligent Human-Machine Systems and Cybernetics, Hangzhou, China, 26–27 August 2015; pp. 260–265.
20. Argenti, F.; Lapini, A.; Bianchi, T.; Alparone, L. A tutorial on speckle reduction in synthetic aperture radar images. *IEEE Geosci. Remote Sens. Mag.* **2013**, *1*, 6–35. [CrossRef]
21. Muruganantham, P.; Wibowo, S.; Grandhi, S.; Samrat, N.H.; Islam, N. A systematic literature review on crop yield prediction with deep learning and remote sensing. *Remote Sens.* **2022**, *14*, 1990. [CrossRef]
22. Ali, A.M.; Abouelghar, M.; Belal, A.A.; Saleh, N.; Yones, M.; Selim, A.I.; Amin, M.E.S.; Elwesemy, A.; Kucher, D.E.; Maginan, S.; et al. Crop yield prediction using multi sensors remote sensing. *Egypt. J. Remote Sens. Space Sci.* **2022**, *25*, 711–716.
23. Hosseini, M.; Becker-Reshef, I.; Sahajpal, R.; Lafluf, P.; Leale, G.; Puricelli, E.; Skakun, S.; McNairn, H. Soybean yield forecast using dual-polarimetric C-band synthetic aperture radar. *ISPRS Ann. Photogramm. Remote Sens. Spatial Inf. Sci.* **2022**, *3*, 405–410. [CrossRef]
24. Hashemi, M.G.; Tan, P.N.; Jalilvand, E.; Wilke, B.; Alemohammad, H.; Das, N.N. Yield estimation from SAR data using patch-based deep learning and machine learning techniques. *Comput. Electron. Agric.* **2024**, *226*, 109340. [CrossRef]
25. Maldaner, L.F.; Canata, T.F.; Molin, J.P. An approach to sugarcane yield estimation using sensors in the harvester and Zigbee technology. *Sugar Tech.* **2022**, *24*, 813–821. [CrossRef]

26. Jin, X.; Yang, G.; Xu, X.; Yang, H.; Feng, H.; Li, Z.; Shen, J.; Lan, Y.; Zhao, C. Combined multi-temporal optical and radar parameters for estimating LAI and biomass in winter wheat using HJ and RADARSAT-2 data. *Remote Sens.* **2015**, *7*, 13251–13272. [CrossRef]

27. Kross, A.; Znoj, E.; Callegari, D.; Kaur, G.; Sunohara, M.; Lapen, D.R.; McNairn, H. Using artificial neural networks and remotely sensed data to evaluate the relative importance of variables for prediction of within-field corn and soybean yields. *Remote Sens.* **2020**, *12*, 2230. [CrossRef]

28. Filipponi, F. Sentinel-1 GRD preprocessing workflow. *Proceedings* **2019**, *18*, 11. [CrossRef]

29. Lee, J.S.; Pottier, E. *Polarimetric Radar Imaging: From Basics to Applications*; CRC Press: New York, NY, USA, 2009; p. 398.

30. Oldoni, L.V.; Sanches, I. D.A.; Prudente, V. H.R.; Vieira, D.C.; Gama, F.F. Caracterização da dinâmica da soja, milho e algodão com base em dados SAR polarimétricos do Sentinel-1A. In Proceedings of the Anais do XIX Simpósio Brasileiro de Sensoriamento Remoto, Santos, Brazil, 14–17 April 2019; pp. 692–695.

31. Bouchemakh, L.; Smara, Y.; Boutarfa, S.; Hamadache, Z. A comparative study of speckle filtering in polarimetric radar SAR images. In Proceedings of the 3rd International Conference on Information and Communication Technologies: From Theory to Applications, Damascus, Syria, 7–11 April 2008; pp. 1–6.

32. Lee, J.S. A simple speckle smoothing algorithm for synthetic aperture radar images. *IEEE Trans. Syst. Man Cybern.* **1983**, *1*, 85–89. [CrossRef]

33. Lopes, A.; Nezry, E.; Touzi, R.; Laur, H. Maximum a posteriori speckle filtering and first order texture models in SAR images. In Proceedings of the IGARSS'90, College Park, MD, USA, 20–24 May 1990; Volume 3, pp. 2409–2412.

34. Lee, J.S.; Wen, J.H.; Ainsworth, T.L.; Chen, K.S.; Chen, A.J. Improved sigma filter for speckle filtering of SAR imagery. *IEEE Trans. Geosci. Remote Sens.* **2009**, *47*, 202–213.

35. Amaral, L.R.; Oldoni, H.; Baptista, G.M.; Ferreira, G.H.; Freitas, R.G.; Martins, C.L.; Santos, A.F. Remote Sensing Imagery to Predict Soybean Yield: A Case Study of Vegetation Indices Contribution. *Precis. Agric.* **2024**, *25*, 2375–2393. [CrossRef]

36. Santos, E.P.; da Silva, D.D.; do Amaral, C.H. Vegetation cover monitoring in tropical regions using SAR-C dual-polarization index: Seasonal and spatial influences. *Int. J. Remote Sens.* **2021**, *42*, 7581–7609. [CrossRef]

37. Mitchard, E.T.A.; Saatchi, S.S.; White, L.J.T.; Abernethy, K.A.; Jeffery, K.J.; Lewis, S.L.; Collins, M.; Lefsky, M.A.; Leal, M.E.; Woodhouse, I.H.; et al. Mapping tropical forest biomass with radar and spaceborne LiDAR in Lopé National Park, Gabon: Overcoming problems of high biomass and persistent cloud. *Biogeosciences* **2012**, *9*, 179–191. [CrossRef]

38. Hird, J.N.; DeLancey, E.R.; McDermid, G.J.; Kariyeva, J. Google Earth Engine, open-access satellite data, and machine learning in support of large-area probabilistic wetland mapping. *Remote Sens.* **2017**, *9*, 1310. [CrossRef]

39. Trudel, M.; Charbonneau, F.; Leconte, R. Using RADARSAT-2 polarimetric and ENVISAT-ASAR dual-polarization data for estimating soil moisture over agricultural fields. *Can. J. Remote Sens.* **2012**, *38*, 514–527.

40. Huete, A.; Justice, C.; Van Leeuwen, W. MODIS vegetation index (MOD13). *Algorithm Theor. Basis Doc.* **1999**, *3*, 295–309.

41. Mandal, K.G.; Hati, K.M.; Misra, A.K. Biomass yield and energy analysis of soybean production in relation to fertilizer-NPK and organic manure. *Biomass Bioenergy* **2009**, *33*, 1670–1679. [CrossRef]

42. Martins, C.L.; Santos, A.C.; Canatta, J.V.; Ranzani, G. Classification of the occurrence of broadleaf weeds in narrow-leaf crops. *Eng. Agrícola* **2024**, *44*, e20230148. [CrossRef]

43. Foucher, S.; López-Martínez, C. Analysis, evaluation, and comparison of polarimetric SAR speckle filtering techniques. *IEEE Trans. Image Process.* **2014**, *23*, 1751–1764. [CrossRef]

44. Bipin, C.; Rao, C.V.; Sridevi, P.V. Speckle aware spatial search based segmentation algorithm for crop classification in SAR images using a three component K-NN model. *J. Appl. Remote Sens.* **2023**, *17*, 048503. [CrossRef]

45. Shitole, S.; De, S.; Rao, Y.S.; Pandey, P.C. Selection of suitable window size for speckle reduction and deblurring using SOFM in polarimetric SAR images. *J. Indian Soc. Remote Sens.* **2015**, *43*, 739–750. [CrossRef]

46. McNairn, H.; Kross, A.; Lapen, D.; Caves, R.; Shang, J. Early season monitoring of corn and soybeans with TerraSAR-X and RADARSAT-2. *Int. J. Appl. Earth Obs. Geoinf.* **2014**, *28*, 252–259. [CrossRef]

47. Le Toan, T.; Ribbes, F.; Wang, L.F.; Floury, N.; Ding, K.H.; Kong, J.A.; Fujita, M.; Kurosu, T. Rice crop mapping and monitoring using ERS-1 data based on experiment and modeling results. *IEEE Trans. Geosci. Remote Sens.* **1997**, *35*, 41–56. [CrossRef]

48. McNairn, H.; Brisco, B. The application of C-band polarimetric SAR for agriculture: A review. *Can. J. Remote Sens.* **2004**, *30*, 525–542. [CrossRef]

49. Haldar, D.; Dave, R.; Dave, V.A. Evaluation of full-polarimetric parameters for vegetation monitoring in rabi (winter) season. *Egypt. J. Remote Sens. Space Sci.* **2018**, *21*, S67–S73. [CrossRef]

50. Kim, Y.; Van Zyl, J.J. A time-series approach to estimate soil moisture using polarimetric radar data. *IEEE Trans. Geosci. Remote Sens.* **2009**, *47*, 2519–2527.

51. Maity, S.; Patnaik, C.; Parihar, J.S.; Panigrahy, S.; Reddy, K.A. Study of physical phenomena of vegetation using polarimetric scattering indices and entropy. *IEEE J. Sel. Top. Appl. Earth Obs. Remote Sens.* **2010**, *4*, 432–438. [CrossRef]

52. Hair, J.F.; Black, W.C.; Babin, B.J.; Anderson, R.E.; Tatham, R.L. *Multivariate Data Analysis*, 7th ed.; Pearson Education: Hoboken, NJ, USA, 2009.

53. Jiao, X.; McNairn, H.; Shang, J.; Pattey, E.; Liu, J.; Champagne, C. The sensitivity of RADARSAT-2 polarimetric SAR data to corn and soybean leaf area index. *Can. J. Remote Sens.* **2011**, *37*, 69–81. [CrossRef]

54. Cable, J.W.; Kovacs, J.M.; Jiao, X.; Shang, J. Agricultural monitoring in northeastern Ontario, Canada, using multi-temporal polarimetric RADARSAT-2 data. *Remote Sens.* **2014**, *6*, 2343–2371. [CrossRef]

55. Liu, C.; Shang, J.; Vachon, P. W.; McNairn, H. Multiyear crop monitoring using polarimetric RADARSAT-2 data. *IEEE Trans. Geosci. Remote Sens.* **2012**, *51*, 2227–2240. [CrossRef]

56. Ulaby, F.T. *Microwave Remote Sensing Fundamentals and Radiometry*; Artech House: Reading, MA, USA, 1981.

57. Mermoz, S.; Réjou-Méchain, M.; Villard, L.; Le Toan, T.; Rossi, V.; Gourlet-Fleury, S. Decrease of L-band SAR backscatter with biomass of dense forests. *Remote Sens. Environ.* **2015**, *159*, 307–317. [CrossRef]

58. Bhogapurapu, N.; Dey, S.; Bhattacharya, A.; Mandal, D.; Lopez-Sanchez, J.M.; McNairn, H.; López-Martínez, C.; Rao, Y.S. Dual-polarimetric descriptors from Sentinel-1 GRD SAR data for crop growth assessment. *ISPRS J. Photogramm. Remote Sens.* **2021**, *178*, 20–35. [CrossRef]

59. Shang, J.; Jiao, X.; McNairn, H.; Kovacs, J.; Walters, D.; Ma, B.; Geng, X. Tracking crop phenological development of spring wheat using synthetic aperture radar (SAR) in northern Ontario, Canada. In Proceedings of the 2013 Second International Conference on Agro-Geoinformatics (Agro-Geoinformatics), Fairfax, VA, USA, 12–16 August 2013; pp. 517–521.

60. Nasirzadehdizaji, R.; Cakir, Z.; Sanli, F.B.; Abdikan, S.; Pepe, A.; Calo, F. Sentinel-1 interferometric coherence and backscattering analysis for crop monitoring. *Comput. Electron. Agric.* **2021**, *185*, 106118. [CrossRef]